

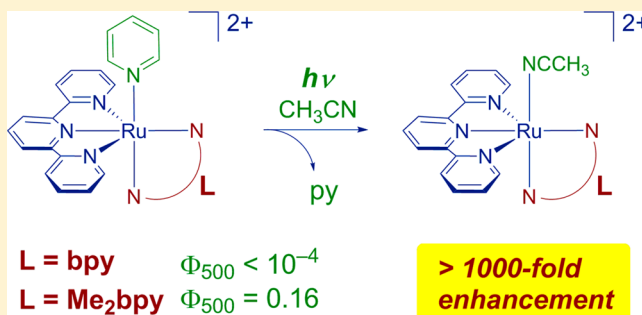
# Unusually Efficient Pyridine Photodissociation from Ru(II) Complexes with Sterically Bulky Bidentate Ancillary Ligands

Jessica D. Knoll, Bryan A. Albani, Christopher B. Durr, and Claudia Turro\*

Department of Chemistry and Biochemistry, The Ohio State University, Columbus, Ohio 43210, United States

## Supporting Information

**ABSTRACT:** The introduction of steric bulk to the bidentate ligand in  $[\text{Ru}(\text{tpy})(\text{bpy})(\text{py})]^{2+}$  (**1**; tpy = 2,2':2'',6''-terpyridine; bpy = 2,2'-bipyridine; py = pyridine) to provide  $[\text{Ru}(\text{tpy})(\text{Me}_2\text{bpy})(\text{py})]^{2+}$  (**2**; Me<sub>2</sub>bpy = 6,6'-dimethyl-2,2'-bipyridine) and  $[\text{Ru}(\text{tpy})(\text{biq})(\text{py})]^{2+}$  (**3**; biq = 2,2'-biquinoline) facilitates photoinduced dissociation of pyridine with visible light. Upon irradiation of **2** and **3** in CH<sub>3</sub>CN ( $\lambda_{\text{irr}} = 500$  nm), ligand exchange occurs to produce the corresponding  $[\text{Ru}(\text{tpy})(\text{NN})(\text{NCCH}_3)]^{2+}$  (NN = Me<sub>2</sub>bpy, biq) complex with quantum yields,  $\Phi_{500}$ , of 0.16(1) and 0.033(1) for **2** and **3**, respectively. These values represent an increase in efficiency of the reaction by 2–3 orders of magnitude as compared to that of **1**,  $\Phi_{500} < 0.0001$ , under similar experimental conditions. The photolysis of **2** and **3** in H<sub>2</sub>O with low energy light to produce  $[\text{Ru}(\text{tpy})(\text{NN})(\text{OH}_2)]^{2+}$  (NN = Me<sub>2</sub>bpy, biq) also proceeds rapidly ( $\lambda_{\text{irr}} > 590$  nm). Complexes **1–3** are stable in the dark in both CH<sub>3</sub>CN and H<sub>2</sub>O under similar experimental conditions. X-ray crystal structures and theoretical calculations highlight significant distortion of the planes of the bidentate ligands in **2** and **3** relative to that of **1**. The crystallographic dihedral angles defined by the bidentate ligand, Me<sub>2</sub>bpy in **2** and biq in **3**, and the tpy ligand were determined to be 67.87° and 61.89°, respectively, whereas only a small distortion from the octahedral geometry is observed between bpy and tpy in **1**, 83.34°. The steric bulk afforded by Me<sub>2</sub>bpy and biq also result in major distortions of the pyridine ligand in **2** and **3**, respectively, relative to **1**, which are believed to weaken its  $\sigma$ -bonding and  $\pi$ -back-bonding to the metal and play a crucial role in the efficiency of the photoinduced ligand exchange. The ability of **2** and **3** to undergo ligand exchange with  $\lambda_{\text{irr}} > 590$  nm makes them potential candidates to build photochemotherapeutic agents for the delivery of drugs with pyridine binding groups.



## INTRODUCTION

The photochemistry of Ru(II) complexes plays an important role in fields that include photochemotherapy (PCT), molecular devices and switches, and solar energy conversion.<sup>1–8</sup>

Ru(II)–polypyridyl complexes are commonly employed in these schemes due to their relatively strong absorption throughout the ultraviolet and visible spectral regions, chemical stability in solution, and their long excited state lifetimes and reactivity that is inaccessible in the ground state.<sup>9,10</sup> The population of the metal-to-ligand charge transfer (<sup>1</sup>MLCT) excited state in these complexes following absorption of a photon is known to undergo fast intersystem crossing to the corresponding <sup>3</sup>MLCT state; in  $[\text{Ru}(\text{bpy})_3]^{2+}$  (bpy = 2,2'-bipyridine) within 15–40 fs.<sup>11,12</sup> The <sup>3</sup>MLCT state can decay via radiative or nonradiative processes to the ground state or may populate thermally accessible triplet ligand field (<sup>3</sup>LF) state(s). Because the <sup>3</sup>LF state exhibits Ru–L( $\sigma^*$ ) character (L = ligand), it can be tuned and exploited to promote efficient ligand dissociation.<sup>13–17</sup>

Complexes related to  $[\text{Ru}(\text{tpy})(\text{bpy})(\text{L})]^{2+}$  (tpy = 2,2':2'',6''-terpyridine; L = monodentate ligand) have been employed for applications such as light-activated drug delivery and photocatalysis.<sup>18,19</sup> For example, the photoisomerization from S-

bound to O-bound dmso for a series of  $[\text{Ru}(\text{tpy})(\text{L}')(\text{dmso})]^{2+}$  complexes (dmso = dimethyl sulfoxide, L' = bidentate ligand) has been used for potential applications in information storage because the compounds are photochromic.<sup>20–22</sup> In these systems, the S → O isomerization proceeds with a quantum yield ( $\Phi_{\text{S} \rightarrow \text{O}}$ ) dependent on the  $\pi$ -donor strength of the atom positioned *trans* to the dmso ligand, with values of 0.25(1), 0.024(1), and 0.007(1) for the complexes with L' = pic (picolinate), bpy, and tmen (N,N,N',N'-tetramethylethylenediamine), respectively.<sup>20–22</sup>

Similarly, the irradiation of the related complex  $[\text{Ru}(\text{tpy})(\text{bpy})(\text{CH}_3\text{CN})]^{2+}$  with visible light in CH<sub>3</sub>CN in the presence of 1 M pyridine produces  $[\text{Ru}(\text{tpy})(\text{bpy})(\text{py})]^{2+}$  (py = pyridine) with  $\Phi = 0.0013$  ( $\lambda_{\text{irr}} = 464$  nm).<sup>23,24</sup> An important point of interest is that the photorelease of pyridine in  $[\text{Ru}(\text{tpy})(\text{bpy})(\text{py})]^{2+}$  is a significantly less efficient process because pyridine forms a stronger bond with Ru(II), such that monodentate ligand dissociation in the excited state is less

**Special Issue:** Current Topics in Photochemistry

**Received:** June 10, 2014

**Revised:** July 15, 2014

**Published:** July 15, 2014

favorable in the py complex than in the corresponding  $\text{CH}_3\text{CN}$  system. This difference is evident in experiments that show that the irradiation of  $[\text{Ru}(\text{tpy})(\text{bpy})(\text{L})]^{2+}$  ( $\text{L} = \text{py}, \text{CH}_3\text{CN}$ ) in DMF to generate  $[\text{Ru}(\text{tpy})(\text{bpy})(\text{DMF})]^{2+}$ . This process occurs with  $\Phi < 10^{-5}$  for  $\text{L} = \text{py}$  but is orders of magnitude more efficient for  $\text{L} = \text{CH}_3\text{CN}$ , with  $\Phi = 0.006$  ( $\lambda_{\text{irr}} = 436 \text{ nm}$ ) under similar experimental conditions.<sup>25</sup> Due to the inefficiency and exhaustive photolysis required, applications involving the photodissociation of pyridine-containing ligands coordinated to  $\text{Ru}(\text{II})$  has been largely impractical to date.

The addition of steric bulk to the ligand set in  $\text{Ru}(\text{II})$  complexes provides a means to distort the pseudo-octahedral geometry around the metal, which has been shown to enhance the efficiency of the excited state ligand exchange.<sup>26,27</sup> The synthesis of  $[\text{Ru}(\text{tpy})(\text{NN})(\text{py})]^{2+}$  complexes with steric bulk on the bidentate NN ligand has been published, although the photoinduced pyridine exchange in these motifs remains largely unexplored. Related work on a series of sterically bulky complexes for the photoinduced release of nitriles in the presence of pyridine was reported.<sup>23</sup> The irradiation of  $[\text{Ru}(\text{Bu-tpy})(\text{phen})(\text{MeOBN})]^{2+}$  ( $\text{Bu-tpy} = 4'-(3,5\text{-ditertibutyl})\text{-phenyl-}2,2',6',2''\text{-terpyridine}$ ;  $\text{MeOBN} = 2,6\text{-dimethoxybenzonitrile}$ ;  $\text{phen} = 1,10\text{-phenanthroline}$ ) with 476 nm promotes the exchange of  $\text{MeOBN}$  with pyridine to produce  $[\text{Ru}(\text{Bu-tpy})(\text{phen})(\text{py})]^{2+}$ . A 20-fold increase in efficiency of this process was observed when the analogous  $[\text{Ru}(\text{Bu-tpy})(\text{Me}_2\text{phen})(\text{MeOBN})]^{2+}$  complex was used under similar experimental conditions, which contains the sterically bulky  $\text{Me}_2\text{phen}$  ( $\text{Me}_2\text{phen} = 2,9\text{-dimethyl-}1,10\text{-phenanthroline}$ ) ligand. In addition, the release of pyridine from  $[\text{Ru}(\text{tpy})(\text{Me}_2\text{bpy})(\text{py})]^{2+}$  ( $\text{tpy} = 4'\text{-tolyl-}2,2':6',2''\text{-terpyridine}$ ,  $\text{Me}_2\text{bpy} = 6,6'\text{-dimethyl-}2,2'\text{-bipyridine}$ ) in  $\text{CH}_3\text{CN}$  to produce  $[\text{Ru}(\text{tpy})(\text{Me}_2\text{bpy})(\text{CH}_3\text{CN})]^{2+}$  was reported, although few details were provided.<sup>28</sup>

The present work focuses on the investigation of two new complexes related to  $[\text{Ru}(\text{tpy})(\text{bpy})(\text{py})]^{2+}$  (**1**), but with additional steric bulk on the bidentate ligand,  $[\text{Ru}(\text{tpy})(\text{Me}_2\text{bpy})(\text{py})]^{2+}$  (**2**) and  $[\text{Ru}(\text{tpy})(\text{biq})(\text{py})]^{2+}$  (**3**;  $\text{biq} = 2,2'\text{-biquinoline}$ ). The structures of the three complexes are depicted in Figure 1. The  $-\text{CH}_3$  substituents on **2** are positioned toward the center of the molecule to strain the pseudo-octahedral geometry around the metal for efficient pyridine exchange. In addition to the steric demands of the biq ligand in **3**, the low-lying biq acceptor orbitals serve to red shift the <sup>1</sup>MLCT absorption maximum, an important factor in PCT to achieve tissue penetration.<sup>29</sup> A spectroscopic analysis of the photolysis of **1–3** in  $\text{CH}_3\text{CN}$  and  $\text{H}_2\text{O}$  are provided, and the quantum yields of pyridine exchange are discussed in relation to the distortion induced by sterically demanding bidentate ligands as determined from X-ray crystal structures and theoretical calculations.

## EXPERIMENTAL SECTION

**Materials.** All materials were used as received without further purification. Pyridine was acquired from Mallinckrodt Chemicals, ammonium hexafluorophosphate and deuterated acetone were purchased from Aldrich, diethyl ether and acetonitrile were obtained from Fisher Scientific, and 200 proof ethanol was purchased from Decon Laboratories. The complexes  $[\text{Ru}(\text{tpy})(\text{Me}_2\text{bpy})\text{Cl}](\text{PF}_6)$ ,<sup>30</sup>  $[\text{Ru}(\text{tpy})(\text{biq})\text{Cl}](\text{PF}_6)$ ,<sup>31</sup> and  $[\text{Ru}(\text{tpy})(\text{bpy})(\text{py})](\text{PF}_6)_2$  (**1**)<sup>24</sup> were prepared by literature methods.

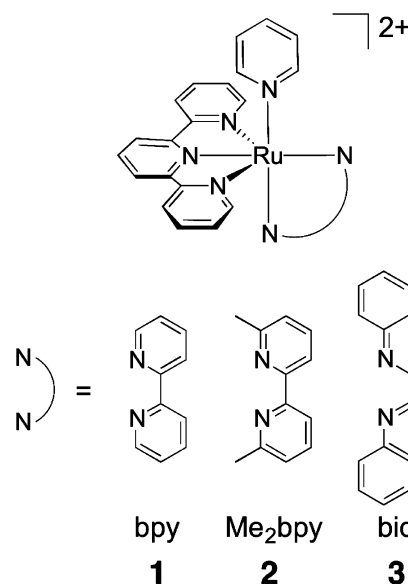


**Figure 1.** Schematic representation of the  $[\text{Ru}(\text{tpy})(\text{NN})(\text{py})]^{2+}$  complexes with the structures of the bidentate NN ligands bpy,  $\text{Me}_2\text{bpy}$ , and biq in **1**, **2**, and **3**, respectively.

**$[\text{Ru}(\text{tpy})(\text{Me}_2\text{bpy})(\text{py})](\text{PF}_6)_2$  (**2**).**  $[\text{Ru}(\text{tpy})(\text{Me}_2\text{bpy})\text{Cl}](\text{PF}_6)$  (0.040 g, 0.057 mmol) and an excess of pyridine (1 mL) in 10 mL of ethanol and 10 mL of  $\text{H}_2\text{O}$  were heated at reflux for 16 h. The reaction mixture was cooled to room temperature, and the ethanol was removed under reduced pressure. Excess  $\text{NH}_4\text{PF}_6$  (0.1 g) was added to the reaction mixture to induce precipitation, and the orange solid was collected by vacuum filtration. The product was washed with 30 mL of  $\text{H}_2\text{O}$  and 30 mL of diethyl ether (0.045 g, 90% yield). The  $\text{Cl}^-$  salt was obtained by ion exchange with an Amberlite column and eluted with methanol. <sup>1</sup>H NMR (400 MHz) in  $(\text{CD}_3)_2\text{CO}$ ,  $\delta$  ppm (splitting, integration): 8.78 (dd, 3H), 8.70 (m, 2H), 8.52 (m, 1H), 8.45 (ddd, 2H), 8.32 (q, 2H), 8.21 (td, 2H), 7.88 (m, 2H), 7.81 (m, 3H), 7.68 (ddd, 2H), 7.19 (dd, 2H), 7.07 (d, 1H), 2.12 (s, 3H), 1.59 (s, 3H).

**$[\text{Ru}(\text{tpy})(\text{biq})(\text{py})](\text{PF}_6)_2$  (**3**).**  $[\text{Ru}(\text{tpy})(\text{biq})(\text{py})](\text{PF}_6)_2$  was prepared following the above procedure and substituting  $[\text{Ru}(\text{tpy})(\text{biq})\text{Cl}](\text{PF}_6)$  (0.03 g, 0.039 mmol) for  $[\text{Ru}(\text{tpy})(\text{Me}_2\text{bpy})\text{Cl}](\text{PF}_6)$  (0.033 g, 88% yield). <sup>1</sup>H NMR (400 MHz) in  $(\text{CD}_3)_2\text{CO}$ ,  $\delta$  ppm (splitting, integration): 9.27 (d, 1H), 9.12 (dd, 1H), 9.02 (d, 1H), 8.94 (d, 2H), 8.73 (m, 2H), 8.55 (m, 1H), 8.43 (m, 2H), 8.30 (ddd, 2H), 8.13 (td, 2H), 7.92 (m, 3H), 7.76 (m, 2H), 7.54 (m, 3H), 7.42 (m, 1H), 7.35 (m, 2H), 7.11 (dd, 2H), 6.89 (dd, 1H).

**Instrumentation.** The <sup>1</sup>H NMR spectra were collected with a Bruker 400 MHz DPX spectrometer. Electronic absorption spectroscopy was performed with a Hewlett-Packard 8453 diode array spectrophotometer. A 150 W Xe arc lamp (USHIO) in a Milliarc lamp housing unit with an LPS-220 power supply and an LPS-221 igniter (PTI) was used for photolysis experiments. The appropriate irradiation wavelengths were selected with a bandpass filter (Thorlabs) and long-pass filter (CVI Melles Griot).

**Methods.** <sup>1</sup>H NMR spectroscopy of **1–3** was performed in acetone- $d_6$ , and the resonances were referenced to the residual acetone signal. Electronic absorption spectroscopy was measured in acetone,  $\text{CH}_3\text{CN}$ , and  $\text{H}_2\text{O}$  at room temperature in a  $1 \times 1 \text{ cm}$  quart cuvette. In the  $\text{H}_2\text{O}$  photolysis experiments, the samples were absorbance matched at 600 nm ( $A = 0.075$ ).

so that the solutions absorb a similar quantity of photons. The quantum yields ( $\Phi$ ) for pyridine dissociation were determined in  $\text{CH}_3\text{CN}$  with an irradiation wavelength of 500 nm. The rate of moles reacted at early irradiation times was determined by monitoring the decrease in the MLCT absorption maximum as a function of time. The photon flux of the lamp with a 435 nm long-pass filter and a 500 nm bandpass filter was determined using ferrioxalate actinometry as previously described in detail, resulting in a flux of  $5.06 \pm 0.31$  mol photons/min.<sup>32</sup>

Single crystals of **2** and **3** were isolated as rod-like and chunk-like red crystals, respectively, and handled under a pool of fluorinated oil. Examination of the diffraction pattern was done on a Nonius Kappa CCD diffractometer with  $\text{Mo K}\alpha$  radiation. All work was conducted at 150 K using an Oxford Cryosystems Cryostream Cooler. Data integration was performed with Denzo, and scaling and merging of the data were done with Scalepack.<sup>33</sup> The structures were solved by the direct methods program in SHELXS-13.<sup>34</sup> Full-matrix least-squares refinements based on  $F^2$  were performed in SHELXL-13,<sup>34</sup> as incorporated in the WinGX package.<sup>35</sup> For each methyl group, the hydrogen atoms were added at calculated positions using a riding model with  $U(\text{H}) = 1.5U_{\text{eq}}$  (bonded carbon atom). The rest of the hydrogen atoms were included in the model at calculated positions using a riding model with  $U(\text{H}) = 1.2U_{\text{eq}}$  (bonded atom). Neutral atom scattering factors were used and include terms for anomalous dispersion.<sup>36</sup>

The structure of **2** had a disordered diethyl ether molecule that had crystallized on an inversion center. To model this disorder, each atom was assigned an occupancy of 50%, which allowed the symmetry operator to generate the second half of the molecule. The atoms were left in their isotropic state as modeling them anisotropically led to an unstable refinement. The structure of **3** also contained highly disordered solvent in the lattice. Modeling of this residual electron density was not straightforward, and despite several attempts at refinement, the solvent molecules remained unstable. The residual density was removed from the model using the SQUEEZE<sup>37</sup> protocol in PLATON,<sup>38</sup> which ultimately removed 67 electrons from a solvent accessible void of 196 Å<sup>3</sup> and corresponds to diethyl ether, a solvent used in crystallization. The CIF file in the Supporting Information provides a description of how **2** was modeled, and Table S1 (Supporting Information) provides crystallographic data collection parameters for **2** and **3**.

Calculations were performed with density functional theory (DFT) using the Gaussian 09 program.<sup>39</sup> The B3LYP<sup>40–42</sup> functional along with the 6-31G\* basis set for H, C, and N<sup>43</sup> and the SDD energy consistent pseudopotentials were used for Ru.<sup>44</sup> Optimization of full geometries was carried out with the respective programs, and orbital analysis was performed in Gaussview version 3.09.<sup>45</sup> Following optimization of the molecular structures, frequency analysis was performed to ensure the existence of local minima on the potential energy surfaces. Electronic absorption singlet to singlet transitions were calculated using time-dependent DFT (TD-DFT) methods with the polarizable continuum model (PCM) that mimicked the solvation effect of  $\text{CH}_3\text{CN}$  in Gaussian 09.<sup>46</sup>

## RESULTS AND DISCUSSION

The electronic absorption spectra of the series of complexes  $[\text{Ru}(\text{tpy})(\text{NN})(\text{py})]^{2+}$ , where NN = bpy (**1**),  $\text{Me}_2\text{bpy}$  (**2**), and biq (**3**), are shown in Figure 2. In general, the spectra of **1–3** feature  $^1\pi\pi^*$  transitions associated with tpy and the NN bidentate ligands in the UV region and  $\text{Ru}(\text{d}\pi) \rightarrow \text{tpy}/\text{NN}(\pi^*)$

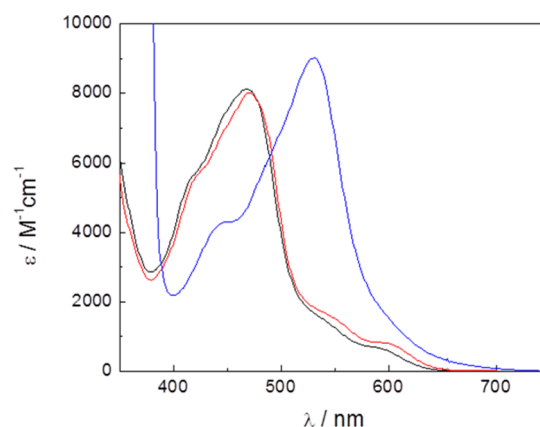


**Figure 2.** Electronic absorption spectra of **1** (black), **2** (red), and **3** (blue) in acetone.

$^1\text{MLCT}$  transitions in the visible range, both of which are typical of  $\text{Ru}(\text{II})$ –polypyridyl complexes.<sup>9</sup> In the case of **1** and **2**, the lowest energy  $^1\text{MLCT}$  transitions are centered at 468 nm ( $\epsilon = 8120 \text{ M}^{-1} \text{ cm}^{-1}$ ) and 471 nm ( $\epsilon = 8020 \text{ M}^{-1} \text{ cm}^{-1}$ ) in acetone, respectively. The reported absorption maximum of **1** in  $\text{CH}_3\text{CN}$  of 467 nm is in sound agreement with the present observations.<sup>24</sup> In contrast, the lowest energy band of **3** is red-shifted compared to those of **1** and **2**, with a maximum at 530 nm ( $\epsilon = 9020 \text{ M}^{-1} \text{ cm}^{-1}$ ). The stabilized biq  $\pi^*$  orbitals relative to those of bpy,  $\text{Me}_2\text{bpy}$ , and tpy shift the  $^1\text{MLCT}$  absorption to lower energy. The lowest energy absorption peaks in **1** and **2** have contributions from both  $\text{Ru} \rightarrow \text{bpy}/\text{Me}_2\text{bpy}$  and  $\text{Ru} \rightarrow \text{tpy}$  MLCT transitions,<sup>24</sup> and the red shift observed for **3** clearly indicates that the lowest energy transition is  $\text{Ru} \rightarrow \text{biq}$  MLCT due to stabilized biq  $\pi^*$  orbitals relative to those of bpy,  $\text{Me}_2\text{bpy}$ , and tpy.<sup>47</sup> For comparison, the lowest energy  $\text{Ru}(\text{II}) \rightarrow \text{biq}$  transition of  $[\text{Ru}(\text{bpy})_2(\text{biq})]^{2+}$  is centered at 525 nm in EtOH/MeOH solution, similar to the maximum of **3** (Figure 2).<sup>48</sup> The stronger absorption of **3** in the low energy tail ( $\lambda > 600 \text{ nm}$ ) represents a promising feature for the application of the complex as a photoactivated drug delivery vehicle because low energy light (600–900 nm) is necessary to penetrate tissue for targeted drug delivery.

The photosubstitution of pyridine in **1–3** with  $\text{CH}_3\text{CN}$  was investigated to compare the efficiency of ligand exchange as a function of the identity of the bidentate ligand. In the dark, **1–3** do not undergo ligand exchange in  $\text{CH}_3\text{CN}$  (Figures S1–S3, Supporting Information), but clear changes in the electronic absorption spectra are observed for **2** and **3** upon irradiation with visible light in  $\text{CH}_3\text{CN}$ , resulting in a blue shift in the  $^1\text{MLCT}$  maximum from 470 to 454 nm in **2** (Figure 3a) and from 529 to 513 nm for **3** (Figure 3b). These shifts correspond to 750 and 590  $\text{cm}^{-1}$  for **2** and **3**, respectively, which are similar to the 610  $\text{cm}^{-1}$  difference between the absorption maxima of **1** and  $[\text{Ru}(\text{tpy})(\text{bpy})(\text{NCCH}_3)]^{2+}$ .<sup>24</sup> The resulting spectra are consistent with the substitution of pyridine with a  $\text{CH}_3\text{CN}$  ligand to form  $[\text{Ru}(\text{tpy})(\text{Me}_2\text{bpy})(\text{NCCH}_3)]^{2+}$  and  $[\text{Ru}(\text{tpy})(\text{biq})(\text{NCCH}_3)]^{2+}$ , respectively. This ligand exchange occurs quite rapidly, within 2 and 4 min of irradiation for **2** and **3**, respectively ( $\lambda_{\text{irr}} > 395 \text{ nm}$ ). The multiple isosbestic points observed for each complex as a function of irradiation time, at 385, 415, and 462 nm for **2** and at 392, 425, 457, and 513 nm for **3**, indicate the formation of a single photoproduct in each reaction. Very little change is observed in the spectrum of **1** on the same time scale (Figure S4, Supporting Information).



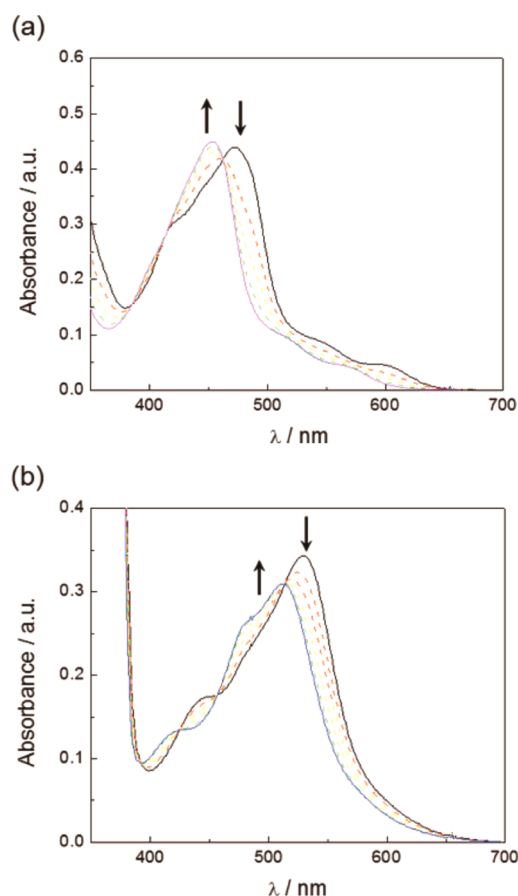


**Figure 3.** Changes in the electronic absorption spectroscopy in  $\text{CH}_3\text{CN}$  with  $\lambda_{\text{irr}} > 395$  nm of (a)  $50 \mu\text{M}$  **2** for  $t_{\text{irr}} = 0, 0.25, 0.5, 1$ , and  $2$  min and (b)  $40 \mu\text{M}$  **3** for  $t_{\text{irr}} = 0, 0.25, 0.5, 1, 2$ , and  $4$  min.

The quantum yield ( $\Phi_{500}$ ) of pyridine dissociation to form the corresponding  $[\text{Ru}(\text{tpy})(\text{NN})(\text{NCCH}_3)]^{2+}$  species was determined to be  $0.16(1)$  and  $0.03(1)$  for **2** and **3** ( $\lambda_{\text{irr}} = 500$  nm), respectively, whereas the analogous pyridine exchange in **1** occurs with  $\Phi_{500} < 0.0001$  (Table 1). The low efficiency

**Table 1.** Absorption Maxima and Photoinduced Ligand Substitution Quantum Yields ( $\Phi$ ) for **1–3**

complex	$\lambda_{\text{abs}}/\text{nm}$ ( $\epsilon/\text{M}^{-1}\text{cm}^{-1}$ ) <sup>a</sup>	$\Phi_{500}$ <sup>b</sup>
$[\text{Ru}(\text{tpy})(\text{bpy})(\text{py})](\text{PF}_6)_2$ ( <b>1</b> )	468 (8120)	<0.0001
$[\text{Ru}(\text{tpy})(\text{Me}_2\text{bpy})(\text{py})](\text{PF}_6)_2$ ( <b>2</b> )	471 (8020)	$0.16 \pm 0.01$
$[\text{Ru}(\text{tpy})(\text{biq})(\text{py})](\text{PF}_6)_2$ ( <b>3</b> )	530 (9020)	$0.033 \pm 0.001$

<sup>a</sup>Measured in acetone at room temperature. <sup>b</sup>Measured in  $\text{CH}_3\text{CN}$ .  $\lambda_{\text{irr}} = 500$  nm.

measured for **1** is consistent with the reported quantum yield for DMF substitution of  $\Phi < 10^{-5}$  upon irradiation ( $\lambda_{\text{irr}} = 436$  nm).<sup>25</sup> It should be noted that the quantum yields observed for **2** and **3** are remarkably large for the photodissociation of a pyridine ligand with low energy visible light. For  $[\text{Ru}(\text{bpy})_2(\text{py})_2]^{2+}$ , the photoinduced ligand exchange of one py ligand with  $\text{Cl}^-$  in  $\text{CH}_3\text{CN}$  was reported to take place with  $\Phi_{436} = 0.0059$ , and the introduction of  $-\text{CH}_3$  groups to produce  $[\text{Ru}(4,4'-\text{Me}_2\text{bpy})_2(\text{py})_2]^{2+}$  ( $4,4'-\text{Me}_2\text{bpy} = 4,4'$ -dimethyl-2,2'-bipyridine) resulted in  $\Phi_{436} = 0.025$  under similar experimental conditions.<sup>49</sup> The 4.2-fold increase in ligand exchange quantum

yield is primarily a result of electronic effects from the electron-donating  $-\text{CH}_3$  substituents. An electronic effect from the  $-\text{CH}_3$  groups in **2** is expected, but the significantly larger  $\Phi$  enhancement for **2** relative to **1** measured in the present work ( $>1600$ -fold; Table 1) indicates that the steric effects of the bulky NN ligand influence the photoreactivity to a much greater extent than electronic effects alone. Moreover, the efficiency of the reaction measured for **2** is  $\sim 4$ -fold greater than the  $\text{Cl}^-$  ligand exchange reported for  $[\text{Ru}(\text{tpy})(\text{py})_3]^{2+}$  and *cis*- $[\text{Ru}(\text{tpy})(\text{py})_2\text{Cl}]^+$  ( $\lambda_{\text{irr}} = 436$  nm).<sup>49,50</sup>

Irradiation of **2** and **3** with low energy light ( $\lambda > 590$  nm) also promotes pyridine substitution in aqueous solution. This activity is important for potential photochemotherapeutic applications, as discussed above. The photolysis of **2** and **3** in  $\text{H}_2\text{O}$  results in a red shift of the MLCT transition, consistent with substitution of the pyridine ligand with a solvent  $\text{H}_2\text{O}$  molecule to form the corresponding  $[\text{Ru}(\text{tpy})(\text{NN})(\text{OH}_2)]^{2+}$  complex. The changes in the electronic absorption spectra of **2** and **3** as a function of irradiation time are displayed in Figure 4a,b, respectively. Photolysis of **2** in  $\text{H}_2\text{O}$  shifts the MLCT

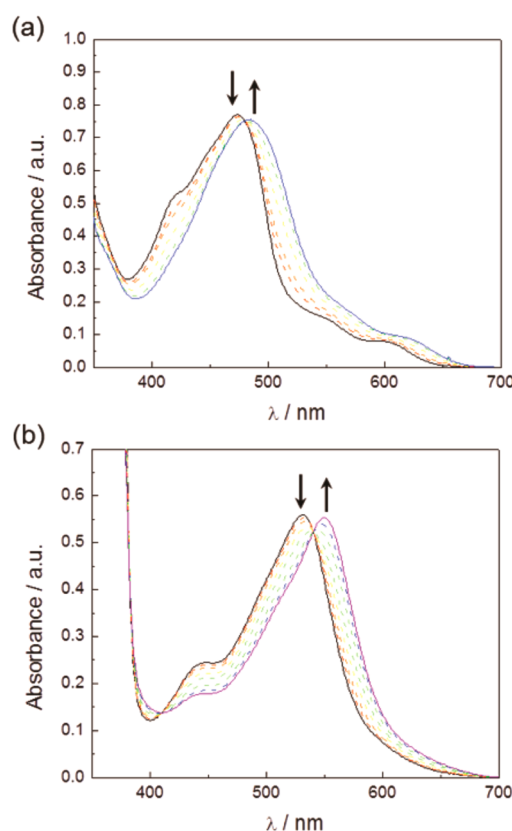


**Figure 4.** Changes in the electronic absorption spectroscopy in  $\text{H}_2\text{O}$  with  $\lambda_{\text{irr}} > 590$  nm of (a)  $94 \mu\text{M}$  **2** for  $t_{\text{irr}} = 0, 1, 3, 7, 15$ , and  $30$  min and (b)  $62 \mu\text{M}$  **3** for  $t_{\text{irr}} = 0, 3, 7, 15, 25, 45, 75$ , and  $100$  min.

absorption from  $473$  to  $485$  nm with an isosbestic point at  $483$  nm, resulting in a spectrum that is in sound agreement with that reported for  $[\text{Ru}(\text{tpy})(\text{Me}_2\text{bpy})(\text{OH}_2)]^{2+}$ .<sup>30</sup> A similar trend is observed for **3**, in which the MLCT absorption shifts from  $530$  to  $548$  nm with isosbestic points at  $408$  and  $540$  nm, and the spectrum of the photoproduct is consistent with that of  $[\text{Ru}(\text{tpy})(\text{biq})(\text{OH}_2)]^{2+}$ .<sup>47</sup> Although this conversion for **2** and **3** occurs on a relatively short time scale (within  $30$  and  $100$  min, respectively), no spectral changes are observed for **1** after

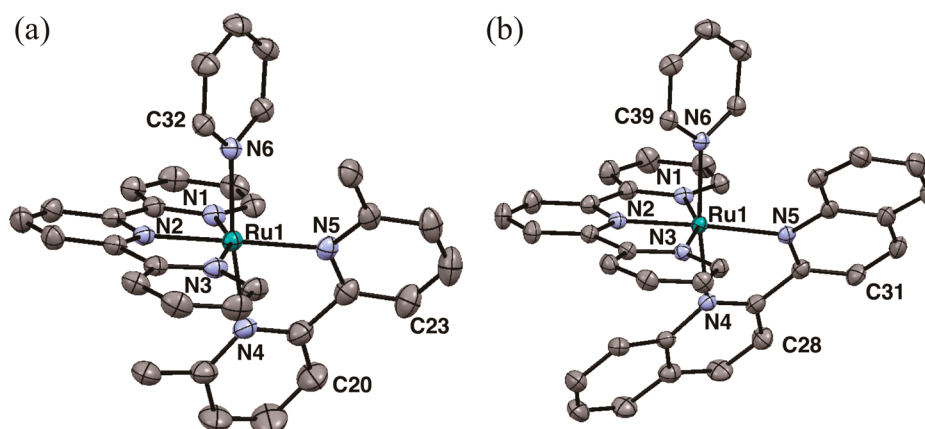


**Figure 5.** ORTEP plots of (a) **2** and (b) **3** (light blue = ruthenium, dark blue = nitrogen, gray = carbon) drawn at 50% probability with selected atom numbers; solvent, hydrogens and counteranions removed for clarity.

photolysis for 2 h (Figure S5, Supporting Information). In contrast, complexes **2** and **3** do not undergo ligand substitution in water when kept in the dark (Figures S6 and S7, Supporting Information). The large differences in the efficiency of pyridine photodissociation for **2** and **3** relative to **1** in water are consistent with the analogous  $\text{CH}_3\text{CN}$  experiments.

Structural analysis of **1–3** provides insight into the factors governing the enhanced ligand exchange of **2** and **3** compared to **1**. The numbering scheme for the atoms of interest is depicted in Figure 5 and those for all the atoms in **2** and **3** appear in Figure S8 (Supporting Information), the experimental and calculated Ru–N bond distances are listed in Table 2, and the experimental and calculated N–Ru–N bond angles

**Table 2.** Experimental and Calculated Ru–N Bond Distances ( $\text{\AA}$ )<sup>a</sup>

bond	<b>1</b> <sup>b</sup>	<b>2</b>	<b>3</b>
Ru–N(1)	2.078 (2.11687)	2.093 (2.13791)	2.100 (2.13993)
Ru–N(2)	1.963 (1.99675)	1.968 (1.99583)	1.969 (1.99769)
Ru–N(3)	2.079 (2.12088)	2.073 (2.11131)	2.071 (2.10599)
Ru–N(4)	2.060 (2.09798)	2.108 (2.16194)	2.101 (2.16377)
Ru–N(5)	2.097 (2.12838)	2.110 (2.16756)	2.115 (2.15707)
Ru–N(6)	2.114 (2.17149)	2.100 (2.17036)	2.105 (2.16500)

<sup>a</sup>Entry represents the experimental bond distances with the calculated bond distances in parentheses. <sup>b</sup>Experimental values from ref 24.

are given in Table 3. The crystal structures of **2** and **3** are shown in Figure 5a,b, respectively, and that of **1** was previously reported;<sup>24</sup> the experimental data for all three complexes are provided in Tables 2 and 3 for comparison. The structures predicted by DFT calculations agree well with the structures determined by X-ray crystallography, although the bond distances are calculated to be  $\sim 0.03$ – $0.06$   $\text{\AA}$  longer than the experimental bond lengths. Similar differences between experimental and theoretical bond distances have also been reported for related complexes.<sup>51</sup> The Ru–N bond distances involving the pyridine and tpy ligands are relatively unperturbed upon addition of steric bulk on the bidentate ligand. This effect was previously observed in the monodentate and bidentate bond distances of  $[\text{Ru}(\text{tpy})(\text{phen})(\text{NCCH}_3)]^{2+}$  and  $[\text{Ru}(\text{tpy})(\text{Me}_2\text{phen})(\text{NCCH}_3)]^{2+}$  ( $\text{Me}_2\text{phen}$  = 2,9-dimethyl-1,10-phenanthroline).<sup>51</sup> It is evident from Table 2 that the addition of steric bulk on NN results in an increase in Ru–N(4) and Ru–N(5) bond lengths associated with the bidentate

ligand by  $\sim 0.04$ – $0.05$  and  $\sim 0.01$ – $0.02$   $\text{\AA}$ , respectively, in both **2** and **3** relative to those of **1**.

The strained pseudo-octahedral geometry around the ruthenium center is further highlighted by select bond angle distortions (Table 3). The bite angle of the tpy ligand distorts the bond angles from the  $90^\circ$  (between *cis* positions) and  $180^\circ$  (between *trans* positions) of an ideal octahedral complex. This distortion is evident in the angles associated with the coordinated pyridine units on the tpy ligand in **1**, determined to be  $79.7^\circ$  for N(1)–Ru–N(2) and N(2)–Ru–N(3) and  $159.3^\circ$  for N(1)–Ru–N(3). These angles remain relatively constant in all three complexes, **1–3**, indicating that the bonding of the tridentate tpy ligand to the ruthenium metal is not affected by the steric bulk on the bidentate ligand. In all three complexes, the planes defined by the three Ru–N bonds of tpy and the two Ru–N bonds of the bidentate ligands are nearly orthogonal, as evidenced by the corresponding N(5)–Ru–N(1,3) and N(4)–Ru–N(1–3) angles, which range from  $87.3$  to  $105.5^\circ$  (average =  $95.3^\circ$ ), and N(2)–Ru–N(5), determined to be  $171.9^\circ$  in **1** (Table 3). Similarly, the N(5)–Ru–N(1,3) and N(4)–Ru–N(1–3) angles in **2** range from  $85.6^\circ$  to  $101.6^\circ$ , and from  $83.5^\circ$  to  $102.3^\circ$  in **3**. In addition the N(2)–Ru–N(5) angles were measured to be  $179.1^\circ$  and  $175.6^\circ$  in **2** and **3**, respectively.

Although the Ru–N bond angles and distances do not exhibit significant variation in **1–3**, distortion from planarity and significant tilting is observed in the bidentate ligands due to steric hindrance in **2** and **3**. The angle describing the orientation of the  $\text{Me}_2\text{bpy}$  ligand relative to tpy in **2**, defined by a plane containing the N(4), N(5), C(20), and C(23) atoms of  $\text{Me}_2\text{bpy}$  (Figure 5) and a plane containing the N(1), N(2), and N(3) atoms in the tpy ligand, was determined to be  $67.87^\circ$ . The corresponding angle in **3** was  $61.89^\circ$ , using the big N(4), N(5), C(28), and C(31) atoms to define the plane. For comparison, only a small distortion from the octahedral geometry is observed between the corresponding atoms in the bpy and tpy ligands in **1**,  $83.34^\circ$ . Therefore, an increase in the tpy–NN angle of  $15.47^\circ$  in **2** and  $21.45^\circ$  in **3** are observed relative to the tpy–bpy angle in **1**. These distortions are also evident in the calculated structures of **1–3** shown in Figure 6a–c.

Moreover, the structures of **1–3** reveal a tilt of the bulky bidentate ligands of **2** and **3** that is not present in **1**. In the predicted and experimental structures of **2** and **3**, the bidentate ligands are tilted relative to the position of the bpy ligand in **1**,

Table 3. Selected Experimental and Calculated N–Ru–N Bond Angles (deg)<sup>a</sup>

angle	1 <sup>b</sup>	2	3
N(1)–Ru–N(2)	79.7 (78.93367)	79.09 (78.60459)	79.23 (78.51967)
N(1)–Ru–N(3)	159.3 (157.54944)	158.38 (157.34106)	158.75 (157.37711)
N(1)–Ru–N(4)	93.4 (90.05910)	85.64 (86.04832)	83.50 (85.13957)
N(1)–Ru–N(5)	94.8 (99.91060)	101.58 (100.89314)	98.87 (100.88704)
N(1)–Ru–N(6)	92.6 (92.84075)	86.64 (87.38447)	87.52 (87.00899)
N(2)–Ru–N(3)	79.7 (78.85892)	79.43 (79.06698)	79.52 (79.06023)
N(2)–Ru–N(4)	95.7 (97.99555)	101.36 (102.38031)	98.40 (102.14905)
N(2)–Ru–N(5)	171.9 (175.49285)	179.09 (179.48745)	175.61 (178.80324)
N(2)–Ru–N(6)	91.0 (88.97176)	85.45 (84.40650)	87.84 (85.40323)
N(3)–Ru–N(4)	87.3 (89.78863)	96.13 (95.01373)	99.50 (96.66863)
N(3)–Ru–N(5)	105.5 (101.97659)	99.86 (101.42717)	102.31 (101.47317)
N(3)–Ru–N(6)	89.11 (90.01682)	94.17 (94.24274)	91.81 (94.18247)
N(4)–Ru–N(5)	78.7 (77.61313)	78.11 (77.46026)	77.40 (76.74188)
N(4)–Ru–N(6)	171.8 (172.85640)	168.54 (169.41974)	167.89 (167.77858)
N(5)–Ru–N(6)	95.2 (95.44693)	95.18 (95.68188)	96.06 (95.61424)

<sup>a</sup>Entry represents the experimental bond angles with the calculated bond angles in parentheses. <sup>b</sup>Experimental values from ref 24.

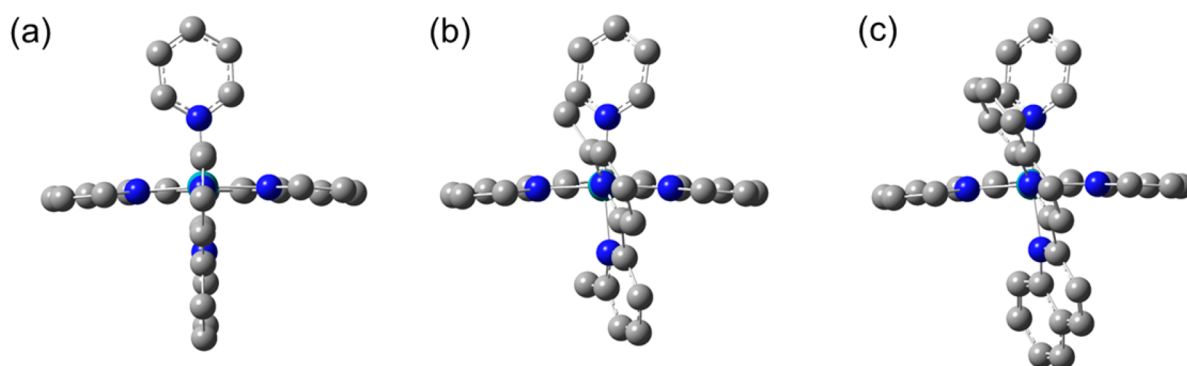


**Figure 6.** Optimized structures predicted by DFT calculations viewed along the axis containing the N(2)–Ru–N(5) bonds for (a) **1**, (b) **2**, and (c) **3**, such that the plane of the tpy ligand is horizontal and that of the bidentate ligand is vertical with respect to the page.

as the  $-\text{CH}_3$  groups of  $\text{Me}_2\text{bpy}$  and the quinoline ligands are oriented toward the N(3) atom on tpy. To compare the tilting of the bidentate ligands in **2** and **3**, one plane was defined by the Ru atom and the N4 and N5 atoms, and a second plane was defined by four atoms on each bidentate ligand (Figure S9, Supporting Information). In **2**, the latter were N4, N5, C20, and C23 on  $\text{Me}_2\text{bpy}$  and in **3** the N4, N5, C28, and C31 atoms of biq were used to define the plane. The resulting tilt angles in the crystal structures of **2** and **3** are  $+20.97^\circ$  and  $+25.88^\circ$ , respectively, which are similar to the calculated values of  $+21^\circ$  in **2** and  $+23^\circ$  in **3**. In contrast, a much smaller tilt is calculated for bpy in **1** and in the opposite direction,  $-6^\circ$ , with a comparable value in the crystal structure,  $-6.75^\circ$ , as expected from its less sterically demanding structure. Overall, the  $\text{Me}_2\text{bpy}$  and biq ligands are more tilted away from the N(4)–Ru–N(5) plane than bpy in **1** by  $\sim 27^\circ$  and  $\sim 32^\circ$  in **2** and **3**, respectively. A similar effect was noted in  $[\text{Ru}(\text{bpy})_2(\text{dmdppz})]^{2+}$  ( $\text{dmdppz}$  = 3,6-dimethyldipyridylphenazine),  $[\text{Ru}(\text{biq})_2(\text{phen})]^{2+}$ , and  $[\text{Ru}(\text{Bu-tpy})(\text{Me}_2\text{phen})(\text{MeOBN})]^{2+}$  in which the  $\text{dmdppz}$ , biq, and  $\text{Me}_2\text{phen}$  ligands tilt approximately  $15^\circ$ ,  $20^\circ$ , and  $23^\circ$ , respectively, due to the steric constraints from the bulky ligands.<sup>23,52,53</sup>

Another major structural difference measured and calculated for **2** and **3** relative to **1** can be found in the tilt of pyridine toward the N(1) and N(2) atoms of the tpy ligand and its rotation about the Ru–N(6) bond. The N(6)–Ru–N(1–3) bond angles listed in Table 3 for **2** and **3** show that the pyridine

ligand is significantly tilted toward the portion of tpy ligand bearing the N(1) and N(2) atoms and away from the N(3) atom. The N(1)–Ru–N(6) and N(2)–Ru–N(6) angles in the crystal structures of **2** and **3** ranged from  $84.45^\circ$  to  $87.84^\circ$ , and are smaller than the same angles in **1**,  $92.6^\circ$  and  $91.0^\circ$ , respectively. In contrast, the N(3)–Ru–N(6) angles in **2** and **3**,  $94.17^\circ$  and  $91.81^\circ$ , respectively, are larger than the  $89.11^\circ$  determined for **1**. Interestingly, the N(6)–Ru–N(4,5) bond angles are largely unaffected by the nature of the bidentate ligand. The optimized geometries of the three complexes shown in Figure 6 provide a visual comparison of the deviations from the predicted  $\sim 90^\circ$  N(6)–Ru–N(1–3) angle in **2** and **3** relative to **1**; this tilt of the pyridine ligand in **2** and **3** is expected to weaken its  $\sigma$ -bonding and  $\pi$ -bonding with the metal relative to **1**.

In addition, both the crystal structure and the calculations show that the rotation of the pyridine about its Ru–N bond deviates significantly in **2** and **3** as compared to that in **1** due to steric constraints imparted by the  $\text{Me}_2\text{bpy}$  and biq ligands. This rotation in the former is clearly evident in the views provided in Figure 6 and is described by the N(2)–Ru–N(6)–C(32) in **2** and the corresponding N(2)–Ru–N(6)–C(39) dihedral angle in **3**, where C(32) and C(39) are the carbon atoms on pyridine pointing toward N(3) on the tpy ligand in each complex. In the crystal structure of **1**, this dihedral angle is  $128.49^\circ$ , a geometry that is expected to provide good orbital overlap for  $\pi$ -back-bonding to the metal. This angle is much larger than the  $56.66^\circ$



and 45.57° dihedral angles in **2** and **3**, respectively, such that overlap between the  $\pi^*$  orbitals of the py group and filled metal  $t_{2g}$ -type orbitals for  $\pi$ -back-bonding is decreased relative to **1**. The dihedral angles measured in the calculated structures, 114.36°, 59.89°, and 52.78° for **1**, **2**, and **3**, respectively, are in good agreement with those from the crystal structures. This rotation of pyridine, taken together with its tilting, is expected to further weaken the Ru(II)–py  $\pi$ -back-bonding in **2** and **3**.

The distorted geometries of **2** and **3** relative to **1** are important for efficient pyridine dissociation. Similar distortions in  $[\text{Ru}(\text{bpy})_2(\text{dmdppz})]^{2+}$ ,  $[\text{Ru}(\text{biq})_2(\text{phen})]^{2+}$ , and  $[\text{Ru}(\text{Bupy})(\text{Me}_2\text{phen})(\text{MeOBN})]^{2+}$  are believed to result in enhanced photoinduced ligand exchange of bulky bidentate ligands.<sup>23,52,53</sup> On the basis of the electronic absorption spectroscopy, the energy of the lowest energy MLCT in **1** and **2** are similar. The significantly distorted geometry for **2** lowers the energy of the  $^3\text{LF}$  state and weakens the Ru–py  $\sigma$ -bond and  $\pi$ -back-bonding, resulting in greater relative population of the  $^3\text{LF}$  state and enhanced ligand dissociation. The geometric distortions are similar for **2** and **3**, but the  $^3\text{LF}$  state in **3** is also predicted to be stabilized relative to that of **1**. However, the MLCT state of **3** is lower in energy than that of **2** due to the lower-lying biq orbitals relative to  $\text{Me}_2\text{bpy}$ , such that the energy difference between the lowest energy  $^3\text{MLCT}$  state and the dissociative  $^3\text{LF}$  state(s) is greater in the former. The larger  $^3\text{MLCT}$ – $^3\text{LF}$  energy gap is expected to result in lower thermal population of the  $^3\text{LF}$  state in **3**, consistent with the observed lower quantum yield for pyridine dissociation. Additionally, the more distorted geometry of the bound pyridine in **2** as compared to **3** may result in smaller overlap in the bonding orbitals in the former, facilitating more efficient pyridine dissociation for **2** in the excited state.

## CONCLUSIONS

Photoinduced pyridine dissociation with greatly enhanced efficiencies over the previously reported **1** was achieved with the bulky bidentate ligands  $\text{Me}_2\text{bpy}$  in **2** and biq in **3**. In  $\text{CH}_3\text{CN}$  solution, pyridine is replaced by a solvent molecule with  $\Phi_{500} = 0.16(1)$  and  $0.033(1)$  for **2** and **3**, respectively, whereas ligand exchange is much less efficient for **1** ( $\Phi_{500} < 0.0001$ ). Although pyridine dissociation is less efficient for **3** than **2**, the red-shifted absorption of **3** is beneficial in developing complexes for drug delivery as red light is optimal for PCT. To this end, low energy light ( $\lambda > 590$  nm) was shown to promote pyridine dissociation in aqueous solution for **2** and **3** on time scales that are inaccessible with **1**. The X-ray crystal structures and theoretical calculations for the three complexes depict significantly more distorted geometries for **2** and **3** compared to **1** due to steric hindrance between the pyridine ligand and the bulky substituent. The Ru–N(6) bond distances are largely unaffected by the addition of steric bulk, suggesting that differences in photoreactivity are influenced by bond angle distortions. These results are important for design considerations for Ru(II) complexes to be used as potential PCT agents, molecular switches/devices, and catalysts. A detailed investigation into the excited state processes involved in pyridine dissociation from Ru(II) complexes with sterically demanding ligands is ongoing.

## ASSOCIATED CONTENT

### Supporting Information

X-ray crystallographic data for **2** and **3**, dark controls in  $\text{CH}_3\text{CN}$  and  $\text{H}_2\text{O}$  for **1**–**3**, UV–vis spectra of photolysis of **1**–**3** in  $\text{CH}_3\text{CN}$  and  $\text{H}_2\text{O}$ , crystal structure numbering scheme, structural representations of ligand tilt angles. Complete ref 39. This material is available free of charge via the Internet at <http://pubs.acs.org>. CCDC 1007458–1007459 contains the supplementary crystallographic data for this paper. These data can be obtained free of charge from The Cambridge Crystallographic Data Center via [www.ccdc.cam.ac.uk/data\\_request/cif](http://www.ccdc.cam.ac.uk/data_request/cif).

## AUTHOR INFORMATION

### Corresponding Author

\*C. Turro. E-mail address: [turro.1@osu.edu](mailto:turro.1@osu.edu).

### Notes

The authors declare no competing financial interest.

## ACKNOWLEDGMENTS

The authors are grateful for the partial support from the National Science Foundation (CHE-1213646) and the National Institutes of Health (RO1-EB016072), and the Ohio Supercomputer Center.

## REFERENCES

- (1) Balzani, V.; Bergamini, G.; Ceroni, P. From the Photochemistry of Coordination Compounds to Light-powered Nanoscale Devices and Machines. *Coord. Chem. Rev.* **2008**, *252*, 2456–2469.
- (2) Balzani, V.; Moggi, L. Photochemistry of Coordination Compounds: A Glance at Past, Present, and Future. *Coord. Chem. Rev.* **1990**, *97*, 313–326.
- (3) Bonnet, S.; Collin, J.-P. Ruthenium-Based Light-Driven Molecular Machine Prototypes: Synthesis and Properties. *Chem. Soc. Rev.* **2008**, *37*, 1207–1217.
- (4) Bruijninx, P. C. A.; Sadler, P. J. Controlling Platinum, Ruthenium, and Osmium Reactivity for Anticancer Drug Design. *Adv. Inorg. Chem.* **2009**, *61*, 1–62.
- (5) Ceroni, P.; Credi, A.; Venturi, M. Light to Investigate (Read) and Operate (Write) Molecular Devices and Machines. *Chem. Soc. Rev.* **2014**, *43*, 4068–4083.
- (6) Grätzel, M. Solar Energy Conversion by Dye-Sensitized Photovoltaic Cells. *Inorg. Chem.* **2005**, *44*, 6841–6851.
- (7) Kalyanasundaram, K.; Graetzel, M. Artificial Photosynthesis: Biomimetic Approaches to Solar Energy Conversion and Storage. *Curr. Opin. Biotechnol.* **2010**, *21*, 298–310.
- (8) Smith, N. A.; Sadler, P. J. Photoactivatable Metal Complexes: From Theory to Applications in Biotechnology and Medicine. *Philos. Trans. R. Soc., A* **2013**, *371*, 20120519.
- (9) Campagna, S.; Puntoriero, F.; Nastasi, F.; Bergamini, G.; Balzani, V., Photochemistry and Photophysics of Coordination Compounds: Ruthenium. In *Photochemistry and Photophysics of Coordination Compounds I*; Balzani, V., Campagna, S., Eds.; Springer: Berlin, Heidelberg, 2007; Vol. 280, pp 117–214.
- (10) Kalyanasundaram, K. Photophysics, Photochemistry and Solar Energy Conversion with Tris(bipyridyl)ruthenium (II) and its Analogues. *Coord. Chem. Rev.* **1982**, *46*, 159–244.
- (11) McCusker, J. K. Femtosecond Absorption Spectroscopy of Transition Metal Charge-Transfer Complexes. *Acc. Chem. Res.* **2003**, *36*, 876–887.
- (12) Cannizzo, A.; van Mourik, F.; Gawelda, W.; Zgrablic, G.; Bressler, C.; Chergui, M. Broadband Femtosecond Fluorescence Spectroscopy of  $[\text{Ru}(\text{bpy})_3]^{2+}$ . *Angew. Chem., Int. Ed. Engl.* **2006**, *45*, 3174–3176.
- (13) Malouf, G.; Ford, P. C. Photochemical Reaction Pathways of Ruthenium(II) Complexes. Evidence Regarding the Reactive Excited

State(s) from Metal-to-Ligand Charge Transfer Excitation of Pentaamine(pyridine)ruthenium(2+) and Related Complexes. *J. Am. Chem. Soc.* **1974**, *96*, 601–603.

(14) Caspar, J. V.; Meyer, T. J. Photochemistry of MLCT Excited States. Effect of Nonchromophoric Ligand Variations on Photochemical Properties in the Series *cis*-Ru(bpy)<sub>2</sub>L<sub>2</sub><sup>2+</sup>. *Inorg. Chem.* **1983**, *22*, 2444–2453.

(15) Durham, B.; Caspar, J. V.; Nagle, J. K.; Meyer, T. J. Photochemistry of Tris(2,2'-bipyridine)ruthenium(2+) Ion. *J. Am. Chem. Soc.* **1982**, *104*, 4803–4810.

(16) Durham, B.; Walsh, J. L.; Carter, C. L.; Meyer, T. J. Synthetic Applications of Photosubstitution Reactions of Poly(pyridyl) Complexes of Ruthenium(II). *Inorg. Chem.* **1980**, *19*, 860–865.

(17) Allen, G. H.; White, R. P.; Rillema, D. P.; Meyer, T. J. Synthetic Control of Excited-State Properties. Tris-Chelate Complexes Containing the Ligands 2,2'-bipyrazine, 2,2'-bipyridine, and 2,2'-bipyrimidine. *J. Am. Chem. Soc.* **1984**, *106*, 2613–2620.

(18) Frasconi, M.; Liu, Z.; Lei, J.; Wu, Y.; Strekalova, E.; Malin, D.; Ambrogio, M. W.; Chen, X.; Botros, Y. Y.; Cryns, V. L.; Sauvage, J. P.; Stoddart, J. F. Photoexpulsion of Surface-Grafted Ruthenium Complexes and Subsequent Release of Cytotoxic Cargos to Cancer Cells from Mesoporous Silica Nanoparticles. *J. Am. Chem. Soc.* **2013**, *135*, 11603–11613.

(19) Bonnet, S.; Limburg, B.; Meeldijk, J. D.; Gebbink, R. J. M. K.; Killian, J. A. Ruthenium-Decorated Lipid Vesicles: Light-Induced Release of [Ru(terpy)(bpy)(OH<sub>2</sub>)]<sup>2+</sup> and Thermal Back Coordination. *J. Am. Chem. Soc.* **2010**, *133*, 252–261.

(20) Rachford, A. A.; Petersen, J. L.; Rack, J. J. Designing Molecular Bistability in Ruthenium Dimethyl Sulfoxide Complexes. *Inorg. Chem.* **2005**, *44*, 8065–8075.

(21) Lutterman, D. A.; Rachford, A. A.; Rack, J. J.; Turro, C. Theoretical Insight on the S → O Photoisomerization of DMSO Complexes of Ru(II). *J. Phys. Chem. A* **2009**, *113*, 11002–11006.

(22) Lutterman, D. A.; Rachford, A. A.; Rack, J. J.; Turro, C. Electronic and Steric Effects on the Photoisomerization of Dimethylsulfoxide Complexes of Ru(II) Containing Picolinate. *J. Phys. Chem. Lett.* **2010**, *1*, 3371–3375.

(23) Bonnet, S.; Collin, J.-P.; Sauvage, J.-P.; Schofield, E. Photochemical Expulsion of the Neutral Monodentate Ligand L in Ru(Terpy\*)(Diimine)(L)<sup>2+</sup>: A Dramatic Effect of the Steric Properties of the Spectator Diimine Ligand. *Inorg. Chem.* **2004**, *43*, 8346–8354.

(24) Hecker, C. R.; Fanwick, P. E.; McMillin, D. R. Evidence for Dissociative Photosubstitution Reactions of [Ru(trpy)(bpy)-(NCCH<sub>3</sub>)]<sup>2+</sup>. Crystal and Molecular Structure of [Ru(trpy)(bpy)-(py)](PF<sub>6</sub>)<sub>2</sub>•(CH<sub>3</sub>)<sub>2</sub>CO. *Inorg. Chem.* **1991**, *30*, 659–666.

(25) Matsubara, Y.; Koga, K.; Kobayashi, A.; Konno, H.; Sakamoto, K.; Morimoto, T.; Ishitani, O. Development of an Efficient and Durable Photocatalytic System for Hydride Reduction of an NAD(P)<sup>+</sup> Model Compound Using a Ruthenium(II) Complex Based on Mechanistic Studies. *J. Am. Chem. Soc.* **2010**, *132*, 10547–10552.

(26) Baranoff, E.; Collin, J.-P.; Furusho, J.; Furusho, Y.; Laemmel, A.-C.; Sauvage, J.-P. Photochemical or Thermal Chelate Exchange in the Ruthenium Coordination Sphere of Complexes of the Ru(phen)<sub>2</sub>L Family (L = Diimine or Dinitrile Ligands). *Inorg. Chem.* **2002**, *41*, 1215–1222.

(27) Laemmel, A.-C.; Collin, J.-P.; Sauvage, J.-P. Efficient and Selective Photochemical Labilization of a Given Bidentate Ligand in Mixed Ruthenium(II) Complexes of the Ru(phen)<sub>2</sub>L<sup>2+</sup> and Ru-(bipy)<sub>2</sub>L<sup>2+</sup> Family (L = Sterically Hindering Chelate). *Eur. J. Inorg. Chem.* **1999**, *1999*, 383–386.

(28) Laemmel, A. C.; Collin, J. P.; Sauvage, J. P. Photosubstitution of Ancillary Ligands in Octahedral Mono-Terpyridine Ruthenium(II) Complexes. *C. R. Acad. Sci. IIC* **2000**, *3*, 43–49.

(29) Szaciłowski, K.; Macyk, W.; Drzewiecka-Matuszek, A.; Brindell, M.; Stochel, G. Bioinorganic Photochemistry: Frontiers and Mechanisms. *Chem. Rev.* **2005**, *105*, 2647–2694.

(30) Bahreman, A.; Limburg, B.; Siegler, M. A.; Bouwman, E.; Bonnet, S. Spontaneous Formation in the Dark, and Visible Light-

Induced Cleavage, of a Ru–S Bond in Water: A Thermodynamic and Kinetic Study. *Inorg. Chem.* **2013**, *52*, 9456–9469.

(31) Bessel, C. A.; Margarucci, J. A.; Acquaye, J. H.; Rubino, R. S.; Crandall, J.; Jircitano, A. J.; Takeuchi, K. J. Steric Ligand Effects of Six Bidentate Bipyridyl Ligands. *Inorg. Chem.* **1993**, *32*, 5779–5784.

(32) Montalti, M.; Credi, A.; Prodi, L.; Gandolfi, M. T. *Handbook of Photochemistry*; CRC press: Boca Raton, FL, USA, 2006.

(33) Otwinowski, Z.; Minor, W. *Methods in Enzymology*, Vol. 276: *Macromolecular Crystallography, Part A*; Academic Press: New York, 1997.

(34) Sheldrick, G. A Short History of SHELX. *Acta Crystallogr., Sect. A* **2008**, *64*, 112–122.

(35) Farrugia, L. J. WinGX suite for Small-Molecule Single-Crystal Crystallography. *J. Appl. Crystallogr.* **1999**, *32*, 837–838.

(36) *International Tables for Crystallography*; Kluwer Academic Publishers: Dordrecht, The Netherlands, 1992.

(37) Sluis, P. v. d.; Spek, A. L. PLATON/SQUEEZE. *Acta Crystallogr., Sect. A* **1990**, *46*, 194–201.

(38) Spek, A. L. Structure Validation in Chemical Crystallography. *Acta Crystallogr., Sect. D* **2009**, *65*, 148–155.

(39) Frisch, M. J.; Trucks, G. W.; Schlegel, H. B.; Scuseria, G. E.; Robb, M. A.; Cheeseman, J. R.; Scalmani, G.; Barone, V.; Mennucci, B.; Petersson, G. A.; et al. *Gaussian 09*, Revision A.1; Gaussian, Inc.: Wallingford, CT, 2009 (full reference in the Supporting Information).

(40) Becke, A. D. Density-Functional Exchange-Energy Approximation with Correct Asymptotic Behavior. *Phys. Rev. A* **1988**, *38*, 3098–3100.

(41) Becke, A. D. Density-Functional Thermochemistry. III. The Role of Exact Exchange. *J. Chem. Phys.* **1993**, *98*, 5648–5652.

(42) Lee, C.; Yang, W.; Parr, R. G. Development of the Colle-Salvetti Correlation-Energy Formula into a Functional of the Electron Density. *Phys. Rev. B* **1988**, *37*, 785–789.

(43) Hehre, W. J.; Radom, L.; Chleyer, P. V.; Pople, J. A. *Ab initio Molecular Orbital Theory*; John Wiley & Sons: New York, 1986.

(44) Andrae, D.; Haeussermann, U.; Dolg, M.; Stoll, H.; Preuss, H. Energy-adjusted ab initio Pseudopotentials for the Second and Third Row Transition Elements. *Theor. Chim. Acta* **1990**, *77*, 123–141.

(45) Dennington II, R.; Keith, T.; Millam, J. *GaussView 3*; Semichem, Inc.: Shawnee Mission, KS, 2007.

(46) Fantacci, S.; De Angelis, F.; Selloni, A. Absorption Spectrum and Solvatochromism of the [Ru(4,4'-COOH-2,2'-bpy)<sub>2</sub>(NCS)<sub>2</sub>] Molecular Dye by Time Dependent Density Functional Theory. *J. Am. Chem. Soc.* **2003**, *125*, 4381–4387.

(47) Klassen, D. M. Excited States of Mixed Ligand Complexes of Ruthenium(II) with 2-(2-Pyridyl)quinoline and 2,2-biquinoline. *Chem. Phys. Lett.* **1982**, *93*, 383–386.

(48) Barigelletti, F.; Juris, A.; Balzani, V.; Belser, P.; Von Zelewsky, A. Excited-State Properties of Complexes of the Tris(diimine)-ruthenium<sup>2+</sup> Ion Family. *Inorg. Chem.* **1983**, *22*, 3335–3339.

(49) Ross, H. B.; Boldaji, M.; Rillema, D. P.; Blanton, C. B.; White, R. P. Photosubstitution in Tris Chelate Complexes of Ruthenium(II) Containing the Ligands 2,2'-bipyrazine, 2,2'-bipyrimidine, 2,2'-bipyridine, and 4,4'-dimethyl-2,2'-bipyridine: Energy Gap Control. *Inorg. Chem.* **1989**, *28*, 1013–1021.

(50) Suen, H. F.; Wilson, S. W.; Pomerantz, M.; Walsh, J. L. Photosubstitution Reactions of Terpyridine Complexes of Ruthenium(II). *Inorg. Chem.* **1989**, *28*, 786–791.

(51) Bossert, J.; Daniel, C. Electronic Absorption Spectroscopy of [Ru(phen)<sub>2</sub>(bpy)]<sup>2+</sup>, [Ru(phen)<sub>2</sub>(dmbp)]<sup>2+</sup>, [Ru(tpy)(phen)-(CH<sub>3</sub>CN)]<sup>2+</sup>, and [Ru(tpy)(dmp)(CH<sub>3</sub>CN)]<sup>2+</sup>. A Theoretical Study. *Coord. Chem. Rev.* **2008**, *252*, 2493–2503.

(52) Wachter, E.; Heidary, D. K.; Howerton, B. S.; Parkin, S.; Glazer, E. C. Light-Activated Ruthenium Complexes Photobind DNA and are Cytotoxic in the Photodynamic Therapy Window. *Chem. Commun.* **2012**, *48*, 9649–9651.

(53) Wachter, E.; Howerton, B. S.; Hall, E. C.; Parkin, S.; Glazer, E. C. A New Type of DNA “Light-Switch”: A Dual Photochemical Sensor and Metalating Agent for Duplex and G-Quadruplex DNA. *Chem. Commun.* **2014**, *50*, 311–313.